

# Structured fabrics with tunable mechanical properties

<https://doi.org/10.1038/s41586-021-03698-7>

Received: 23 August 2020

Accepted: 7 June 2021

Published online: 11 August 2021

 Check for updates

Yifan Wang<sup>1,2,4</sup>, Liuchi Li<sup>1,4</sup>, Douglas Hofmann<sup>3</sup>, José E. Andrade<sup>1</sup> & Chiara Daraio<sup>1✉</sup>

Structured fabrics, such as woven sheets or chain mail armours, derive their properties both from the constitutive materials and their geometry<sup>1,2</sup>. Their design can target desirable characteristics, such as high impact resistance, thermal regulation, or electrical conductivity<sup>3–5</sup>. Once realized, however, the fabrics' properties are usually fixed. Here we demonstrate structured fabrics with tunable bending modulus, consisting of three-dimensional particles arranged into layered chain mails. The chain mails conform to complex shapes<sup>2</sup>, but when pressure is exerted at their boundaries, the particles interlock and the chain mails jam. We show that, with small external pressure (about 93 kilopascals), the sheets become more than 25 times stiffer than in their relaxed configuration. This dramatic increase in bending resistance arises because the interlocking particles have high tensile resistance, unlike what is found for loose granular media. We use discrete-element simulations to relate the chain mail's micro-structure to macroscale properties and to interpret experimental measurements. We find that chain mails, consisting of different non-convex granular particles, undergo a jamming phase transition that is described by a characteristic power-law function akin to the behaviour of conventional convex media. Our work provides routes towards lightweight, tunable and adaptive fabrics, with potential applications in wearable exoskeletons, haptic architectures and reconfigurable medical supports.

Smart fabrics are wearable materials that sense and respond to environmental stimuli, varying their properties<sup>6,7</sup>, and/or measuring and communicating data to external recording devices<sup>5,8</sup>. Their applications include medical monitoring, wearable computing and energy harvesting<sup>5,8–10</sup>. They are usually fabricated by integrating 'smart' components, such as flexible electronic circuits for sensing and computing<sup>5,8,9</sup>, phase-changing materials for thermal regulation<sup>6</sup> or photovoltaic materials for solar energy harvesting<sup>10</sup> into conventional fabrics. However, most of these solutions focus on sensing and data communication. Fabrics with adaptable or tunable mechanical properties could provide mechanical feedback to human bodies and perform functions such as joint assistance, support and haptic perception<sup>11</sup>. Here, we introduce a type of architected fabric, consisting of chain mail layers with designed particles, that can reversibly and gradually switch between soft and rigid states. Such a fabric, with its tunable mechanical properties, is a promising candidate for smart wearable applications.

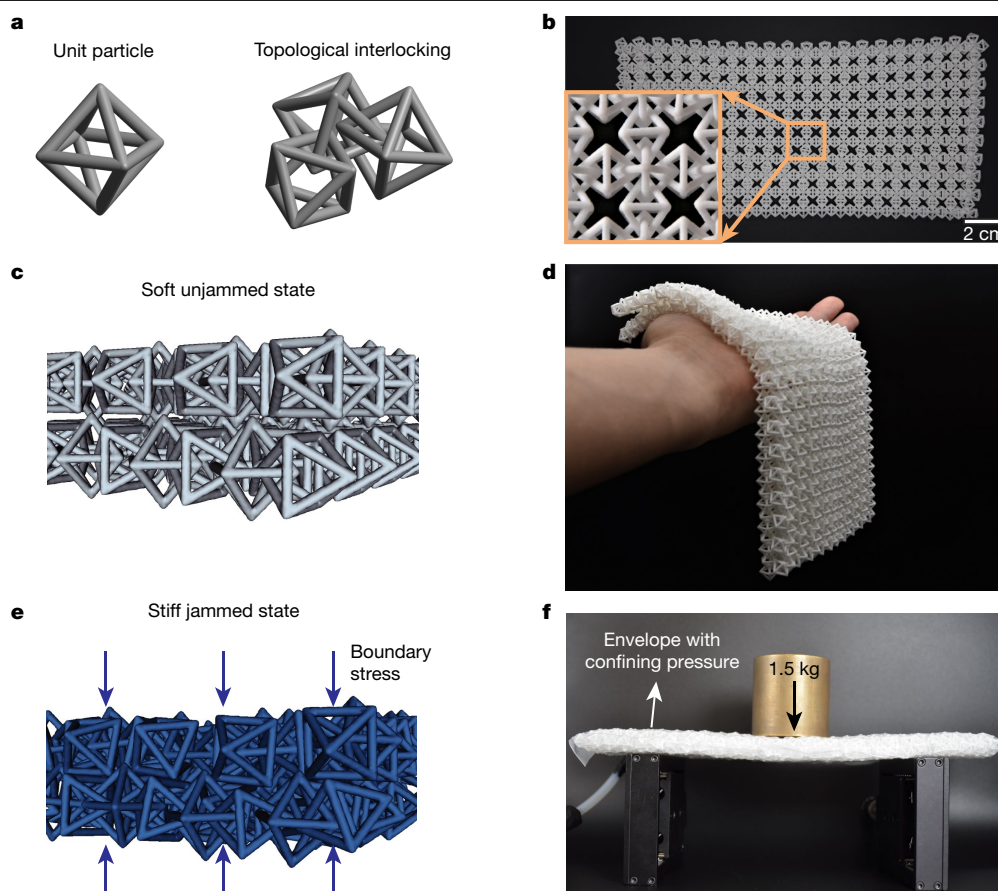
Unlike other fabrics that are woven or knitted with continuous material (such as fibres and wires)<sup>1,8</sup>, the basic building blocks of our designed fabrics are discrete, granular particles. Assemblies of granular particles or laminar structures are known to undergo changes in their mechanical properties during jamming<sup>12–16</sup>. Jamming is a phase transition that does not rely on temperature changes, as in ordinary materials, but is instead controlled by local geometric constraints in granular matter. The jamming transition enables disordered granular systems to switch reversibly between deformation with fluid-like

plasticity or with solid-like rigidity, accompanied by a change of packing fraction. Jamming has been used to create smart materials with adaptive mechanical properties, for example, in soft robotic grippers, impact absorption materials and reconfigurable architectures<sup>17–19</sup>. However, conventional granular materials are dense and large volumes are needed to provide enough mechanical stiffness when jammed. In addition, assemblies of convex particles do not support tensile forces. This limits their bending stiffness and tensile strength, making them unsuitable for wearable fabrics.

## Fabrication and characterization

Inspired by ancient chain mail armour<sup>21,20</sup> and topologically interlocked elements<sup>21,22</sup>, we have designed a structured fabric consisting of two layers of interlocked granular particles. In our material, each particle is a hollow, three-dimensional (3D) structure, constructed from connecting trusses, designed to reduce the overall density and enhance contacts between elements (Fig. 1a). We chose octahedral particles because their 90° rotational symmetry enables the formation of a square 2D lattice in the interlocked configuration, and their sharp corners increase contacts between layers. The chain mail is created by rotating neighbouring particles 90° with respect to each other and by topologically interlocking all particles without forming solid connections. The interlocked lattice is manufactured using a selective laser sintering method, which prints the lattice in one piece without extra

<sup>1</sup>Division of Engineering and Applied Science, California Institute of Technology, Pasadena, CA, USA. <sup>2</sup>School of Mechanical and Aerospace Engineering, Nanyang Technological University, Singapore, Singapore. <sup>3</sup>Jet Propulsion Laboratory/ California Institute of Technology, Pasadena, CA, USA. <sup>4</sup>These authors contributed equally: Yifan Wang, Liuchi Li. ✉e-mail: daraio@caltech.edu



**Fig. 1 | The design and prototype of the architected chain mail fabrics.** **a**, Schematic of a single architected particle (left) and three interlocking particles (right). **b**, A 3D printed chain mail. **c**, Numerical simulation of two chain mail layers, without boundary confining stress. **d**, Digital image of two

chain mail layers in the soft state. **e**, Configuration of the particles shown in **c**, after a confining stress is applied. **f**, Digital image of the jammed chain mails, which become a stiff load-bearing structure.

supports (Fig. 1b). We stack two chain mail layers to increase the number of contacts. Like chain mail armour, the resulting structured sheets can freely bend, fold and drape over curved objects (Fig. 1c, d). We avoid 3D-printing chain mail with particles interlocked through thickness (that is, the two layers are stacked but are not physically linked) to allow sliding between layers, which results in higher flexibility.

To tune the effective mechanical properties of our fabric, we seek to trigger jamming between the interlocked particles, by applying variable compression at the boundary (Fig. 1e, f). We enclose the two layers in an airtight, flexible envelope, where the layers are weakly coupled and can still bend easily. To induce jamming, we apply a confining gauge pressure (pumping air out of the envelope), which causes confinement stress at the fabrics' boundaries. This increases the particles' overall packing fraction, triggering a jamming transition that increases the bending modulus and turns the fabrics into load-bearing structures (Fig. 1f).

To quantify the change in mechanical properties as a function of increasing confining pressure, we perform three-point bending tests and calculate the apparent elastic bending modulus of the fabrics (see Methods). In these experiments, the samples are supported at two edges, and a line-shaped indenter is applied to the centre of the top layer. The measured force–displacement curves ('displacement controlled' in Fig. 2a) show an initially linear regime, at small indentation depths, governed by the elastic behaviour of the jammed granular structure. As indentation increases, a nonlinear response is observed, probably due to frictional sliding and local rearrangement of the particles. Although our fabrics are discrete and strongly anisotropic, we use an apparent elastic bending modulus  $E^*$  as a parameter to compare the

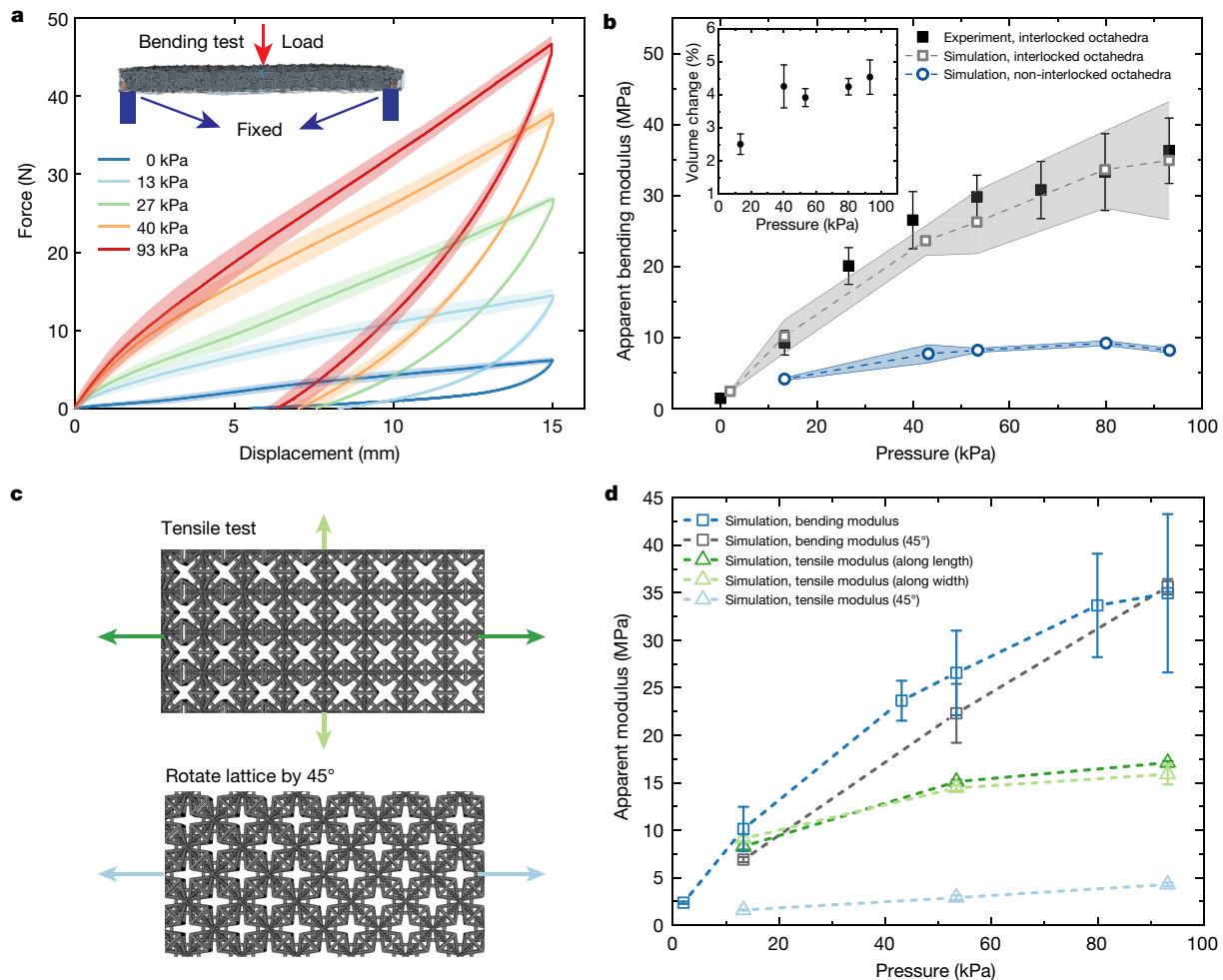
fabrics' mechanical properties under different conditions (see Methods).  $E^*$  can be calculated as<sup>23</sup>:

$$E^* = \frac{KL^3}{4bh^3} \quad (1)$$

Here,  $K$  is the stiffness of the initial elastic regime from the three-point bending test (Fig. 2a), and  $L$ ,  $b$  and  $h$  are the length, width and height of the fabrics before the three-point loading tests (see Methods). As the internal confining pressure increases from 0 kPa to about 93 kPa, the apparent bending modulus increases monotonically, from about 1.4 MPa to about 36.3 MPa (Fig. 2b), by over 25 times. We note that the plateau reached by the apparent bending modulus at high confining pressures (Fig. 2b) depends on our experimental setup (that is, the choice of the envelope). Different confinement solutions may allow higher bending moduli to be reached. It is important to emphasize that the jamming effect is controlled largely by contact topology. Compared to other variable-modulus materials<sup>24,25</sup>, such as shape memory alloys<sup>26,27</sup>, magnetorheological materials<sup>28</sup> or electroactive polymers<sup>29</sup>, our smart fabrics have the advantage of high modulus tunability without the need for applying large temperature changes or high electrical/magnetic fields, which are undesirable in wearable applications.

### Numerical modelling of the fabrics

To understand the fundamental mechanisms leading to the increase in bending stiffness, we study the microstructural interactions and displacements between particles using numerical simulations (Fig. 2a).



**Fig. 2 | Bending and tensile tests with variable confining pressure.**

**a**, Measured force–displacement curves for the fabrics at different confining pressures,  $P$ . The coloured lines represent the average values, and the shaded areas represent the standard deviation between five different tests. **b**, Apparent bending modulus as a function of the confining pressure,  $P$ , comparing experiments and numerical simulations. Simulation results for discrete octahedral particle aggregates (non-interlocked) are also shown (blue circles). The error bars are standard deviations obtained from five separate experiments. The shaded areas in grey and blue are standard deviations obtained from four separate simulations, each of which has a different initial

particle configuration. The inset shows the change of the fabrics' overall volume obtained from four separate simulation results, the inset error bars are standard deviations from these simulations. **c**, Schematic of tensile tests performed along different directions. The bottom fabric consists of a lattice rotated 45° from the lattice at the top (which has loading directions oriented at 0° or 90° along the reference configuration). **d**, Simulations of apparent bending and tensile moduli along various loading directions showing anisotropy. The error bars represent the standard deviation between three simulations with different initial configurations.

Within the range of confining pressures imposed in our experiments, the constituent particles' elastic deformation is much smaller than the particles' rigid body motion (for example, rearrangement) and can be neglected. We model the chain mail architecture as a granular system, using the level set-discrete element method (LS-DEM<sup>30</sup>). LS-DEM can reveal the detailed microstructures formed from granular particles of arbitrary shape<sup>31,32</sup>. We model the fabrics by constructing a 'digital twin' of the hollow octahedral particle (Extended Data Fig. 1a, b), which is then replicated and rearranged to reproduce the 3D-printed fabrics (Extended Data Fig. 1c). We model the flexible envelope used in the experiments as a discretized elastic layer<sup>33</sup> (see Methods and Extended Data Fig. 1c, d). After calibration (see Methods), the model captures the temporal evolution of the dynamics (Extended Data Fig. 2a–c and Supplementary Videos S1 and S2), and quantitatively predicts the fabrics' apparent bending moduli, at different confining pressures (Fig. 2b).

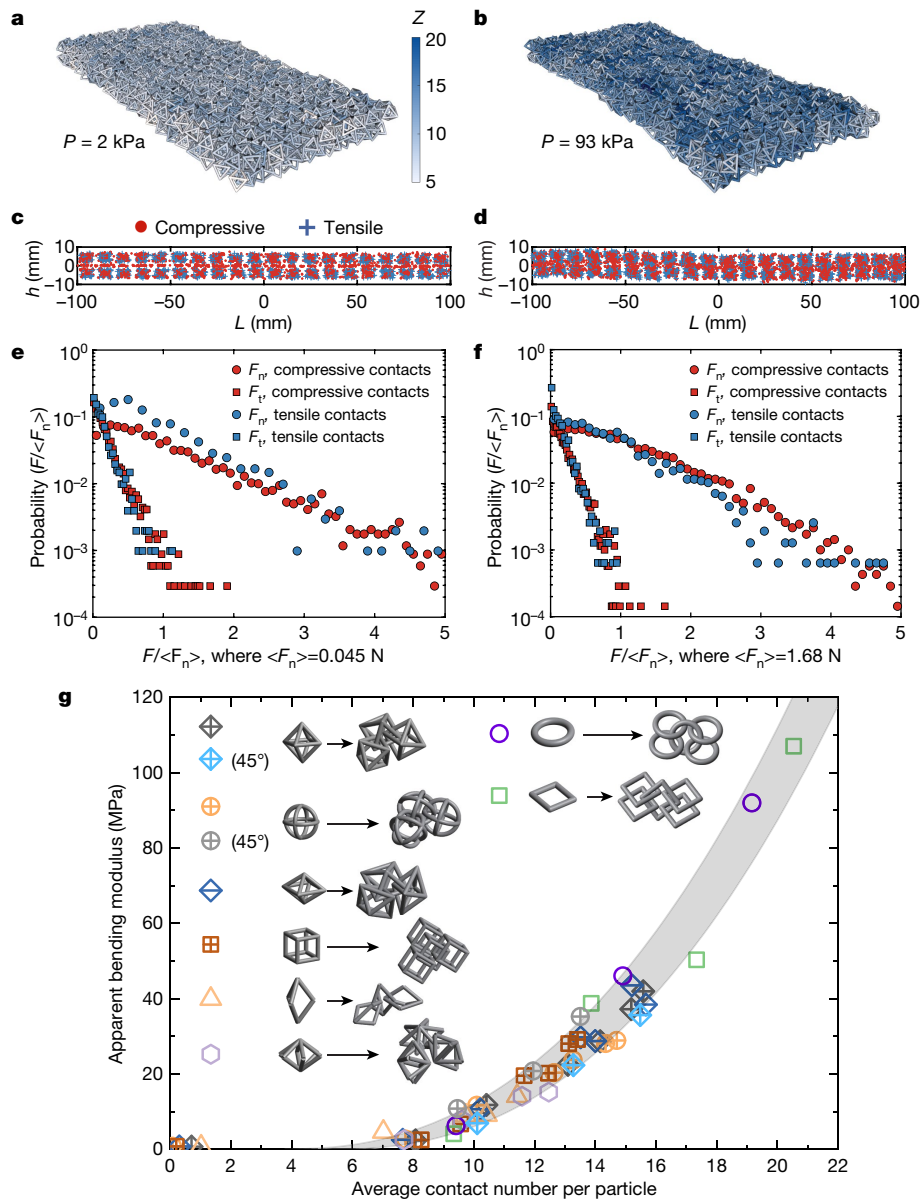
We show that the stiffening of the fabrics requires very small volume shrinkage (below 5%; see inset to Fig. 2b). This is because jamming is a sharp phase transition with a small change in the particle packing fraction<sup>12–15</sup>. As comparison, we perform the same virtual experiments on

assemblies composed of the same hollow octahedrons, but without topological interlocking (see Methods and Extended Data Fig. 1c, d). We observe that interlocked fabrics outperform loose aggregates by exhibiting a higher bending modulus at the same confining pressure (about three times higher; Fig. 2b). This enhancement of modulus at the jammed state can be attributed to the tensile resistance between particles caused by the topological interlocking, which is not present in the loose particle aggregates. In addition, we tested the anisotropy of the fabrics by performing bending and tensile simulations along different directions (Fig. 2c, d). The anisotropy for tensile deformations is much stronger than for bending deformations. This is because the 0°/90° loading direction in the reference configuration are principal directions of the particle connections.

### Relating moduli to microstructures

In jammed granular media, the macroscale mechanical rigidity is directly related to the number of contacts (a microstructural quantity) formed within the system<sup>13</sup>. Constitutive material properties play a secondary part, as long as the particles remain rigid. In our system,





**Fig. 3 | Micro-structural information obtained from simulations at different confining pressures. a, b,** Colour map distribution of the contact number of each particle ( $Z$ ) in the fabrics at  $P = 2$  kPa (**a**) and  $P = 93$  kPa (**b**). **c, d,** Spatial distribution of the compressive and tensile contact points in the fabrics at  $P = 2$  kPa (**c**) and  $P = 93$  kPa (**d**).  $L$ , length;  $h$ , height. **e, f,** Probability distributions of normal and tangential contact forces (normalized by the mean normal force  $\langle F_n \rangle$ ), at  $P = 2$  kPa (**e**) and  $P = 93$  kPa (**f**). **g,** Relation between the apparent elastic bending modulus ( $E^*$ ) and the average contact number per particle ( $\bar{Z}$ ), for eight different particle geometries. The results are fitted to a

power-law scaling with different onset parameter ( $Z_0$ ) represented by the grey-shaded area. The legend shows the symbol representation (left) for each type of particle geometry (middle), and the unit cells (right) for constructing the fabric sheets. The confining pressures used in these plots are 0.1 kPa, 2 kPa, 13 kPa, 43 kPa, 53 kPa, 80 kPa and 93 kPa, respectively, for symbol numbers 1, 3, 5 and 6; 13 kPa, 53 kPa and 93 kPa, respectively, for symbol numbers 2 and 4; 0.1 kPa, 2 kPa, 13 kPa, 43 kPa and 53 kPa, respectively, for symbol numbers 7 and 8; and 0.1 kPa, 13 kPa, 25 kPa and 43 kPa for symbol numbers 9 and 10.

we analyse the variation of contact number for each particle within the fabrics, at different confining pressures. We observe that higher confining pressures induce more interparticle contacts (Fig. 3a, b). We further divide interparticle contacts into ‘compressive’ and ‘tensile’ categories (Extended Data Fig. 2d) and show their spatial distributions under different pressures (Fig. 3c, d). Two observations can be made. (1) ‘Tensile’ contacts encompass clusters of ‘compressive’ contacts in a semi-periodic pattern. This observation can be explained by the specific interlocking topology of the hollow octahedron: tensile contacts (‘tensile type’ in Extended Data Fig. 2d) can only occur near each particle’s vertices, which are far away from the particle’s centroid. Compressive contacts (‘compressive types 2 and 3’ in Extended Data

Fig. 2d) can occur in the void volume occupied by each particle, which are closer to the particle’s centroid. This kind of compressive contact within a particle’s occupied volume is typically not possible in conventional convex granular particles. (2) Interparticle contacts between two fabric layers (near  $h = 0$  in Fig. 3c, d) are all compressive contacts (‘compressive type 1’ in Extended Data Fig. 2d), which is due to the fact that there is no interlocking between fabric layers.

We plot the corresponding probability distribution (see Methods) of the normal ( $F_n$ ) and tangential contact forces ( $F_t$ ), at two different confining pressures (Fig. 3e, f). The observed distribution patterns for both normal and tangential forces are similar to the well established patterns for granular materials composed of conventional convex particles under



isotropic compression<sup>34</sup>. That is, the tangential and normal force distributions both show exponential tails. The normal force distribution is broad around the mean and larger normal forces (those well above the mean) decay faster than forces around the mean. Such distributions also seem to be insensitive to the applied confining pressure, at least for the range considered in our study. Interestingly, the distributions of compressive and tensile contacts are nearly identical, especially when the confining pressure is large (Fig. 3f, where  $P = 93$  kPa). This result suggests that the well established force distribution patterns for conventional, convex granular materials also apply to non-convex granular materials, where tensile contacts can also exist, provided that the imposed boundary conditions are the same (isotropic compression, in this case).

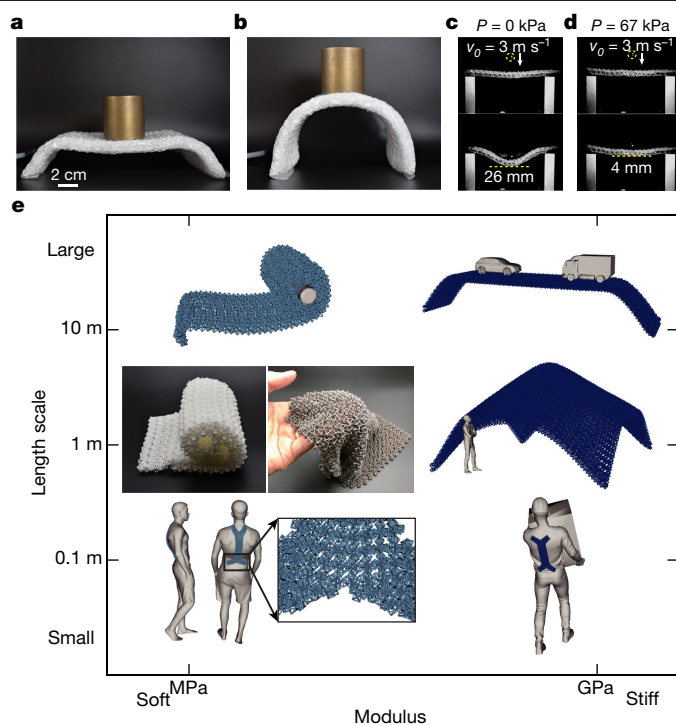
To explore the relation between particle geometry and the jammed structure's mechanical properties, we design five other 3D particle geometries and construct corresponding interlocked fabrics (see Methods and Extended Data Fig. 3). We utilize the validated LS-DEM model to study the mechanical responses of these fabrics under three-point bending tests. For each simulation, conducted under a different confining pressure, we compute the average contact number per particle ( $\bar{Z}$ , summing both compressive and tensile contacts), and the apparent bending modulus ( $E^*$ ) for a beam subjected to three-point bending tests (see Methods). We observe that the apparent bending modulus increases monotonically with the average contact number (Fig. 3g), after a certain onset value  $Z_0$ .  $Z_0$  is defined as the critical contact number required for the granular structure to be structurally rigid<sup>13</sup>. Remarkably, the computed relations between apparent bending modulus and average contact number for different particle geometries all collapse onto the same shaded region (Fig. 3g), which is fitted by adopting a power-law function predicted by the critical phenomenon of the jamming phase transition with different  $Z_0$  onset values (ref.<sup>13</sup>; see Methods and Extended Data Table 1). Interestingly, we observe that the apparent bending moduli measured on fabrics with a rotated lattice (shapes 2 and 4) also follow this scaling trend, with different  $Z_0$  values from the reference configuration. This indicates that the scaling relation is still valid when considering the fabric's anisotropy.

As comparison, we also modelled two-layer stacking of classical chain mail layers consisting of interlocked ring-shaped and square-shaped particles (see Methods and Extended Data Fig. 4). The results from these classical chain mail layers also follow the power-law scaling observed previously (Fig. 3g). Interestingly, at the same confining pressure, stackings of classical chain mail layers (consisting of ring- or square-shaped particles) have higher apparent bending moduli compared to fabrics consisting of 3D structured particles. This is because the classical chain mail layers have a higher packing fraction (over two times larger) than those with 3D structured particles (see Extended Data Table 1). However, the higher packing fraction leads to higher volumetric density. 3D structured particles offer advantages in applications (such as tunable wearable equipment) where light weight may be a priority. In addition, the 3D structured particles with hollow internal volumes enable future incorporation of smart materials (for example, shape memory wires or polymers) for different actuation methods.

By connecting a microscale geometric quantity ( $\bar{Z}$ ) to a macroscale mechanical property ( $E^*$ ), the observed power-law scaling can have practical implications for the rational design of adaptive structured materials aimed at different applications. By customizing the particle shape, the tradeoff between weight and bending modulus tunability can be optimally balanced. In the future, it will be interesting to see whether this power law also holds for fabrics composed of particles with different geometries or made from different constitutive materials, which are not currently considered in this study.

### Shape reconfigurability and impact

Another feature of the fabrics studied is that they can be shaped into different geometries before being jammed into load-bearing structures.



**Fig. 4 | Shape reconfigurability, tunable impact resistance, and applications.** **a**, The fabric, forming a flat table shape under load of 1.5 kg. **b**, The fabric, forming an arch bearing the same load. **c**, **d**, Snapshots from high-speed camera recording of impact tests on fabrics supported at 2 edges, under two different confining pressures:  $P = 0$  kPa (**c**) and  $P = 67$  kPa (**d**). **e**, Possible applications of the reconfigurable fabrics at different length scales, ranging from wearable medical supports and exoskeletons (bottom) to transportable, reconfigurable architectures (top). The two inset images show the fabrics in the soft state, printed with two different materials: nylon plastic (left) and aluminium (right). Images are from <https://www.cgtrader.com/3d-print-models/miniatures/figurines/builder-carries-a-box> and <https://www.cgtrader.com/free-3dmodels/car/suv/porsche-cayenne-3>.

To demonstrate this, we manually configure the fabrics into a flat table (Fig. 4a) and an arch (Fig. 4b) and apply confining pressures. The resulting structures are mechanically stiff and able to bear mechanical loads, over 30 times their own weight. This shaping ability is especially important for wearable applications and reconfigurable structures, where the fabrics may need to conform to the human body or form complex architectures.

The fabrics can also serve as tunable protective layers against particle impacts. We demonstrate this property with drop-weight impact tests, dropping a stainless steel bead (of 30 g mass, 1.27 cm diameter) onto suspended fabrics, with an impact velocity of  $3 \text{ m s}^{-1}$ . We study the strike penetration as a function of the confining pressure imparted on the fabric. The impact process is recorded by a high-speed camera (see Supplementary Videos S3 and S4). The penetration depth of the projectile can be greatly reduced with increased confining internal pressure: from 26 mm at 0 kPa (Fig. 4c) to 4 mm at 67 kPa (Fig. 4d), achieving over six times reduction of the penetration depth.

### Discussion

Our work has systematically explored the mechanics of structured fabrics consisting of non-convex interlocked particles with precisely controlled geometry, during the jamming transition. Reconfigurable fabrics composed of discrete particles can be realized at different

scales, because the jamming transition is a scale-invariant physical phenomenon (Fig. 4e). Recent advances in additive manufacturing make it possible, in principle, to scale the fabric thickness from the micrometre to the metre scales, and to use different constitutive materials (such as metal; see the inset to Fig. 4e), targeting different applications. With the integration of alternative methods for confinement (for example, electrical or magnetic control), it is possible to envision programming stiffness at different locations within the fabrics, for applications such as haptic interfaces and medical stimulation.

## Online content

Any methods, additional references, Nature Research reporting summaries, source data, extended data, supplementary information, acknowledgements, peer review information; details of author contributions and competing interests; and statements of data and code availability are available at <https://doi.org/10.1038/s41586-021-03698-7>.

- Chen, X., Taylor, L. W. & Tsai, L. J. An overview on fabrication of three-dimensional woven fabric preforms for composites. *Text. Res. J.* **81**, 932–944 (2011).
- Engel, J. & Liu, C. Creation of a metallic micromachined chain mail fabric. *J. Micromech. Microeng.* **17**, 551–556 (2007).
- Tabiei, A. & Nilakantan, G. Ballistic impact of dry woven fabric composites: a review. *Appl. Mech. Rev.* **61**, 010801 (2008).
- Cai, L. et al. Warming up human body by nanoporous metallized polyethylene fabric. *Nat. Commun.* **8**, 496 (2017).
- Stoppa, M. & Chiolerio, A. Wearable electronics and smart fabrics: a critical review. *Sensors* **14**, 11957–11992 (2014).
- Mondal, S. Phase change materials for smart fabrics—an overview. *Appl. Therm. Eng.* **28**, 1536–1550 (2008).
- Gauvreau, B. et al. Color-changing and color-tunable photonic bandgap fiber fabrics. *Opt. Express* **16**, 15677–15693 (2008).
- Cherenack, K., Zysset, C., Kinkeldei, T., Münzenrieder, N. & Tröster, G. Woven electronic fibers with sensing and display functions for smart fabrics. *Adv. Mater.* **22**, 5178–5182 (2010).
- Cherenack, K. & van Pieterse, L. Smart fabrics: challenges and opportunities. *J. Appl. Phys.* **112**, 091301 (2012).
- Chen, J. et al. Micro-cable structured fabric for simultaneously harvesting solar and mechanical energy. *Nat. Energy* **1**, 16138 (2016).
- Ploszajski, A. R., Jackson, R., Ransley, M. & Miodownik, M. 4D printing of magnetically functionalized chainmail for exoskeletal biomedical applications. *MRS Adv.* **4**, 1361–1366 (2019).
- Liu, A. J. & Nagel, S. R. Jamming is not just cool any more. *Nature* **396**, 21 (1998).
- Liu, A. J. & Nagel, S. R. The jamming transition and the marginally jammed solid. *Annu. Rev. Condens. Matter Phys.* **1**, 347–369 (2010).
- Bi, D., Zhang, J., Chakraborty, B. & Behringer, R. P. Jamming by shear. *Nature* **480**, 355–358 (2011).
- Jaeger, H. Celebrating *Soft Matter*'s 10th anniversary: toward jamming by design. *Soft Matter* **11**, 12 (2015).
- Narang, Y. S., Vlassak, J. J. & Howe, R. D. Mechanically versatile soft machines through laminar jamming. *Adv. Funct. Mater.* **28**, 1707136 (2018).
- Brown, E. et al. Universal robotic gripper based on the jamming of granular material. *Proc. Natl Acad. Sci. USA* **107**, 18809–18814 (2010).
- Wang, Y. et al. Architected lattices with adaptive energy absorption. *Extreme Mech. Lett.* **33**, 100557 (2019).
- Aejmelaeus-Lindstrom, P., Willmann, J., Tibbitts, S., Gramazio, F. & Kohler, M. Jammed architectural structures: towards large-scale reversible construction. *Granul. Matter* **18**, 28 (2016).
- Brown, E., Nasto, A., Athanassiadis, A. G. & Jaeger, H. M. Strain stiffening in random packings of entangled granular chains. *Phys. Rev. Lett.* **108**, 108302 (2012).
- Dyskin, A. V., Estrin, Y., Kanel-Belov, A. J. & Pasternak, E. A new concept in design of materials and structures: assemblies of interlocked tetrahedron-shaped elements. *Scr. Mater.* **44**, 2689–2694 (2001).
- Dyskin, A. V., Pasternak, E. & Estrin, Y. Mortarless structures based on topological interlocking. *Front. Struct. Civ. Eng.* **6**, 188–197 (2012).
- Zweben, C., Smith, W. & Wardle, M. Test methods for fiber tensile strength, composite flexural modulus, and properties of fabric-reinforced laminates. In *Composite Materials: Testing and Design (Fifth Conference)* 228–262 (1979).
- Manti, M., Cacucciolo, V. & Cianchetti, M. Stiffening in soft robotics: a review of the state of the art. *IEEE Robot. Autom.* **23**, 93–106 (2016).
- Wang, L. et al. Controllable and reversible tuning of material rigidity for robot applications. *Mater. Today* **21**, 563–576 (2018).
- Meng, H. & Li, G. A review of stimuli-responsive shape memory polymer composites. *Polymer* **54**, 2199–2221 (2013).
- White, T. J. & Broer, D. J. Programmable and adaptive mechanics with liquid crystal polymer networks and elastomers. *Nat. Mater.* **14**, 1087–1098 (2015).
- Jackson, J. A. et al. Field responsive mechanical metamaterials. *Sci. Adv.* **4**, eaau6419 (2018).
- Biggs, J. et al. Electroactive polymers: developments of and perspectives for dielectric elastomers. *Angew. Chem. Int. Ed.* **52**, 9409–9421 (2013).
- Kawamoto, R., Andò, E., Viggiani, G. & Andrade, J. E. Level set discrete element method for three-dimensional computations with triaxial case study. *J. Mech. Phys. Solids* **91**, 1–13 (2016).
- Kawamoto, R., Andò, E., Viggiani, G. & Andrade, J. E. All you need is shape: predicting shear banding in sand with LS-DEM. *J. Mech. Phys. Solids* **111**, 375–392 (2018).
- Li, L., Marteau, E. & Andrade, J. Capturing the inter-particle force distribution in granular material using LS-DEM. *Granul. Matter* **21**, 43 (2019).
- Cundall, P. A. & Strack, O. D. L. A discrete numerical model for granular assemblies. *Geotechnique* **29**, 47–65 (1979).
- Majmudar, T. S. & Behringer, R. P. Contact force measurements and stress-induced anisotropy in granular materials. *Nature* **435**, 1079–1082 (2005).

**Publisher's note** Springer Nature remains neutral with regard to jurisdictional claims in published maps and institutional affiliations.

© The Author(s), under exclusive licence to Springer Nature Limited 2021

## Methods

### Experiments

**Materials and manufacturing.** The nylon plastic structured chain mails are 3D printed via selective laser sintering using a commercial 3D printing service (Shapeways). The material used to print the fabric is PA 2200 nylon plastic, with a density of  $0.93 \text{ g cm}^{-3}$ , a tensile modulus of 1.7 GPa and a tensile strength of 48 MPa (<http://www.shapeways.com/materials/versatile-plastic>). The equivalent density of the printed fabric is about  $0.18 \text{ g cm}^{-3}$ , which is lower than most wearable materials. The flexible envelop is made of polyethylene plastic film (McMaster-Carr) with thickness of  $h_m = 0.076 \text{ mm}$  and elastic modulus  $E_m \approx 0.3 \text{ GPa}$ . The membrane's contribution to the measured apparent bending moduli,  $E^*$ , should be no greater than the  $E^*$  measured at near-zero confining pressure (about 1 MPa). At higher confining pressures, the membrane forms wrinkles that substantially reduce the overall tensile resistance and its contribution to the overall bending moduli. Because of the presence of these wrinkles, we neglect the membrane's contribution at higher confining pressures in our analysis. The aluminium chain mails (Fig. 4e) are printed on a metal 3D printer (Electro Optical Systems, EOS M 290) with customized break-away supports. A commercial material aluminium, AlSi10Mg, from EOS is used for printing.

**Quasi-static and impact mechanical tests.** The bending stiffness of the fabrics enclosed within airtight envelopes, at different confining pressures, is characterized with three-point bending tests. The membrane envelope is first placed around the fabrics and the opening is sealed using a heat sealer. A soft tube connects from inside the envelope to a manual vacuum pump with pressure gauge. Different vacuum pressures are applied using the pump and the envelope is then sealed for testing. The membrane naturally wrinkles when the vacuum is applied to conform to the fabric surface, which greatly reduces its resistance upon stretching. The supports of the bending test have a width of 10 mm. We use an Instron E3000 materials tester, displacement controlled at a loading rate of  $0.5 \text{ mm s}^{-1}$ . Five separate tests are repeated at each confining pressure. Before each test, the fabrics are manually reset to a flat initial configuration. The coloured lines and dashed areas in Fig. 2a represent the average values and standard deviations for the five different tests. The deviation observed between the results from different tests at the same pressure arises from the initial configurations of the layers, which have different random initial contacts between the two chain mail layers. In the impact tests, the fabric sheets are suspended between two metal supports at the edges and impacted using a stainless-steel sphere of mass  $m = 30 \text{ g}$ . The impact velocity,  $v_0 = 3 \text{ m s}^{-1}$ , is set by the sphere's initial drop height. The impact is recorded using a high-speed camera (Phantom Vision Research) at a rate of 3,000 frames per second, to track the position of the sphere during impact.

**Calculating the fabric's apparent bending modulus.** The stiffness of the initial elastic regime in our three-point bending measurement was obtained by linearly fitting the force–displacement curve (Fig. 2a) at small indentation depths (0 to 0.5 mm). This small indentation corresponds to an in-plane strain of  $<0.05\%$ , which ensures that the fabrics are deforming within their elastic limit. The overall dimensions ( $L$ ,  $h$  and  $b$ ) of the fabrics in the envelope at different confining pressures are measured before the three-point bending tests. The apparent bending modulus is computed according to equation (1), using the measured dimensions and stiffness (slope) of the elastic regime.

### Numerical simulations

**Construction of each particle's digital twin.** We first construct a digital twin (with the same shape, size and density) of the fabricated hollow octahedron particles. A single digital twin is represented by two sets of points that allow for contact computations between two

particles. The first set of points (termed 'nodes' hereafter), together with their triangulations (the right-hand side image in Extended Data Fig. 1a), characterize the shape of the hollow octahedron in a discretized manner. The points in the second set (termed 'grids' hereafter) are equally spaced in space along all three directions ( $x$ ,  $y$  and  $z$ ), and each grid point stores a signed scalar value (positive if outside the hollow octahedron's surface, zero if on and negative if inside) indicating its shortest distance to the triangulated surface formed by the nodes (Extended Data Fig. 1b). Accordingly, these grid points together with their stored values form a discretized level set representation for the hollow octahedron. To clarify this construction, we also highlight in Extended Data Fig. 1b the grid points (coloured in blue) whose shortest distances to the hollow octahedron's surface is less than 0.01 mm. As expected, these highlighted grid points reproduce the geometry of the hollow octahedron reasonably well.

After constructing the digital twins for all particles, we use them to detect contacts and compute contact forces. We follow the standard penalization formulation adopted in the discrete element method (DEM<sup>33</sup>). That is, a contact between two hollow octahedrons happens if at least one node point of one hollow octahedron (octahedron 'i') penetrates the surface of the other (octahedron 'j'). This is achieved by computing the signed shortest distance of each node point of octahedron 'i' using the grid points (which store a discretized level set function) of octahedron 'j', and selecting node points of octahedron 'i' with negative distances to octahedron 'j' (that is, inside octahedron 'j'). These negative distances are penalized following a linear Hookean model to generate the contact forces at each selected node point. We sum the contact forces induced at all selected node points of octahedron 'i' to get the total contact force between octahedron 'i' and octahedron 'j'. The total contact force is used to update the kinematics of each particle following Newtonian mechanics. For a detailed discussion on the relevant formulation and implementation, we refer to ref.<sup>31</sup>.

Since we directly sum over all contact forces induced at all of the node points that are in contact, as discussed in ref.<sup>32</sup>, it is important to match the resolution of both nodes and grids for different particle geometries, in order to ensure consistent and comparable simulation results for different fabrics.

We start by creating a digital twin of the hollow octahedrons with a certain node and grid resolution. The node resolution is chosen such that the constructed digital twin (Fig. 1c and Fig. 1e and the righthand-side image in Extended Data Fig. 1a) can reasonably capture the major feature of the actual geometry of the hollow octahedron (Figs. 1a, b and the lefthand-side image in Extended Data Fig. 1a). Next, we create the digital twins of all other particle geometries considered with the respective node resolution matching that of the digital twin of the hollow octahedron. Specifically, we match the probability distribution of the triangulation's edge lengths of each particle's digital twin to that of the constructed digital twin of the hollow octahedron (Extended Data Figs. 3 and 4). In this work, we use GMSH (an open-source finite-element mesh generator, <https://www.gmsh.info/>) to create the node component of a digital twin and match the node resolution as described above. Once the node resolution is matched, we find that the number of nodes discretizing each particle scales reasonably well with the total surface area of the respective particle (Extended Data Fig. 3 and Extended Data Fig. 4). This implies a consistent level of spatial discretization homogeneity between different digital twins generated by GMSH. The grid resolution is chosen to be able to resolve the interior and exterior of the hollow octahedron (we choose an intergrid distance of 0.2 mm in all three directions to resolve the truss members' thickness, which is 1 mm, as indicated in the inset to Extended Data Fig. 1b). Taking the generated node component of a digital twin, we use MATLAB (<https://www.mathworks.com/help/matlab/>) to set the grid resolution for all digital twins to be 0.2 mm and generate the grid component of the digital twin. These two components are then merged into a single file, which is used as an input for LS-DEM simulations.



We choose the dimensions of all other particle geometries considered, such that when two fabric sheets are vertically stacked they can be enclosed tightly by the envelope constructed (Extended Data Fig. 1c), and as a consequence, they share, on average, the same total dimensions (height, width and length) as that of the sheets composed of hollow octahedra after isotropic compression. We note that maintaining overall the same dimensions of different sheets is important in our work because the results of three-point bending tests can be sensitive to the geometry and size of the specimen. An additional requirement is that the initial configuration of each sheet produced should be free of interparticle contacts. To satisfy the two stated requirements, we are able to adjust only particle size while maintaining the same truss member thickness (1 mm) for all particle geometries except for the circular and the rectangular ring. For these two geometries, besides adjusting the particle sizes, we further increase the truss member thickness to 3.6 mm for the circular ring and to 2.7 mm for the rectangular ring.

The mass of each chain mail layer measured in experiment is 27 g. When considering gravity, this corresponds to an equivalent pressure of  $(0.027 \text{ kg} \times 9.81 \text{ m s}^{-2}) / (0.21 \text{ m} \times 0.092 \text{ m}) = 13.7 \text{ Pa}$ .

Although this pressure could contribute to the bending modulus at zero, or very low, confining pressures, it can be neglected for confining pressures above 2 kPa. For simplicity, the effect of gravity is not considered in our simulations. All particles share the same density, equal to the density of the material used in the experiments. Once the digital twin is created for each of the particle geometries considered, we replicate and arrange in space these digital twins, to construct the corresponding fabric sheets numerically (Extended Data Figs. 3 and 4). Last, to simplify our calibration process (see Methods section ‘Determining model parameters’, for relevant discussions), we scale the density of every envelope sphere such that they all share the same mass with the hollow octahedron.

**Construction of the envelope.** In the experiments within the small strain limit, we observe that the envelope remains wrinkled and conforms to the particles’ surfaces. As such, we assume that the membrane acts only as a compliant layer that applies the confining pressure, without contributing to the sample’s overall bending stiffness. From this assumption, we construct a simplified envelope model that serves only as a compliant elastic layer to transmit the imposed confining pressure to the fabric. Specifically, we construct an envelope with an initially rectangular box shape, to enclose the fabrics, as in the experiments (Extended Data Fig. 1c). We triangulate the surface of the envelope and assign a sphere at each node and a connection (that is, a normal and a shear spring) at each edge between two neighbouring spheres. Consequently, each sphere is connected to six neighbouring spheres. The resting length of each spring is given by the corresponding initial edge length, while the radius of each sphere is given by the average initial length of the six edges in connection with the sphere. The radius of each sphere is thus different but resides in the range of 0.9 mm to 1.3 mm (Extended Data Fig. 1e). Similarly, the node resolution of the envelope is adjustable and we choose a resolution balancing the trade-off between representation accuracy and computational expense. Again, once a resolution is determined, we use the constructed envelope in all of our simulations for consistency.

For the simulations of non-interlocked, hollow octahedrons, we construct a slightly higher envelope, to enclose loose octahedrons that are initially positioned into three layers with no mutual contacts or links (Extended Data Fig. 1d). This choice is made to ensure that at the jammed state, the samples of loose particles share approximately the same dimensions (height, width and length) as those of the samples of the stacked chain mail layers (Extended Data Table 2). Keeping the same sample dimensions ensures that the results from the simulated three-point bending tests are directly comparable to one another. To use the same model parameters for these two different envelopes, we choose a node resolution for the new envelope, such that the statistical

distribution of the envelope sphere’s radius matches that of the original envelope (Extended Data Fig. 1e).

**Isotropic compression.** A given confining pressure  $P$  is applied to the fabrics by going through each triangle  $i$  of the envelope, computing its area  $A_i$  and inward surface normal  $n_i$ , calculating the total force  $PA_i n_i$  and distributing equally to each of the three connecting envelope spheres (Extended Data Fig. 1c). We iterate the above procedure allowing the whole system to relax to equilibrium. Note that at each iteration the values of  $A_i$  and  $n_i$  are updated following the envelope’s deformation. We monitor the total kinetic energy and total contact number of all particles at each time step, and we deem equilibrium to be achieved if both the total kinetic energy and total contact number cease to show any preferred direction of evolution with time, notwithstanding certain small temporal fluctuations (Extended Data Figs. 2a, b).

**Three-point bending.** After the whole system equilibrates under isotropic compression as described above, we perform three-point bending simulation by changing the boundary condition. In addition to maintaining the imposed isotropic compression, we fix the dynamics of the particles along the two edges of the fabric to the bottom layer (coloured red in Extended Data Fig. 2a). We impose a constant force pointing downward vertically (that is, along the  $z$  direction) that is evenly distributed on particles along the centre line of the fabric on the top layer (coloured blue in Extended Data Fig. 2a). The value of the applied force is chosen according to the experimental results (Fig. 2a), ensuring the simulated mechanical response is within the small strain limit (that is, elastic regime). We iterate the above procedure allowing the whole system to relax to equilibrium under the new boundary condition. The average vertical deflection (along the  $z$  direction) of the loaded particles is monitored in time. We deem equilibrium to be achieved if the average vertical deflection ceases to evolve with time (Extended Data Fig. 2c). Once equilibrium is achieved, we stop the simulation.

**Computing the fabric’s dimension at jammed state.** We define the jammed state in our work as the state of the fabric immediately after the completion of the isotropic compression, before the three-point bending simulation. The height (along  $z$  direction), width (along  $y$  direction) and length (along  $x$  direction) of a given fabric at the jammed state are computed as follows (here we take height as the illustrative example): we first identify and group particles belonging to the top and bottom layers. Next, for each group, we go through each particle within the group, identify the nodal point with the largest (for top layer group) or smallest (for bottom layer group) value along the  $z$  direction, and average along the  $z$  direction all identified nodal points for both the top layer group and bottom layer group. Last, we compute the height as the difference between these two averaged values. For the simulated results of the apparent bending modulus, shown in Fig. 2b, the corresponding height, width and length of both interlocked fabrics and loose assemblies are summarized in Extended Data Table 2.

**Modelling the interactions between particles and envelope spheres.** To describe the model parameters, we use a subscript notation, as follows: we use ‘n’ (‘t’) to represent the normal (tangential) direction for a contact, ‘p’ to represent the particle (for example, the hollow octahedron), ‘s’ to represent the envelope sphere, and ‘-’ to represent the interaction). For example,  $k_{n,p-p}$  means the normal contact stiffness  $k$  between two particles, and  $\gamma_{n,p-s}$  means the normal contact damping  $\gamma$  between a particle and an envelope sphere. Interactions between particles are modelled as being linear Hookean, with Coulomb friction. Associated model parameters are the contact normal (tangential) stiffness  $k_{n,p-p}$  ( $k_{t,p-p}$ ), the contact normal (tangential) viscous damping  $\gamma_{n,p-p}$  ( $\gamma_{t,p-p}$ ) and the friction coefficient  $\mu_{p-p}$ . The viscous damping can be determined from the respective coefficient of restitution  $e_{n,p-p}$  ( $e_{t,p-p}$ ), following  $\gamma_{n,p-p} = -\ln(e_{n,p-p}) \sqrt{m_p k_{n,p-p} / \sqrt{\pi^2 + \ln^2 e_{n,p-p}}}$  (ref. <sup>35</sup>)

# Article

( $\gamma_{t,p-p}$  can be computed analogously using  $e_{t,p-p}$ ). Here  $m_p$  is the mass of a single hollow octahedron. The value of a coefficient of restitution resides between 0 and 1, with 0 indicating perfectly plastic binary collision and 1 indicating perfectly elastic binary collision. Interactions between particles and envelope spheres are also modelled as being linear Hookean, but without any friction. This frictionless assumption is a reasonable approximation since the envelope used in the experiments is compliant enough to conform to the surface of the particles upon isotropic compression. Associated model parameters are contact normal stiffness  $k_{n,p-s}$  and contact normal viscous damping  $\gamma_{n,p-s}$  (where  $\gamma_{n,p-s}$  can be determined from  $e_{n,p-s}$ ). Last, for the interactions between envelope spheres, each envelope sphere only interacts with its six nearest neighbours via the connecting normal and shear spring. Since the envelope used in the experiments is very compliant to shear and compression but resistive to tension, we use three parameters to describe the behaviour of the spring: normal compressive stiffness  $k_{n,compressive}$ , normal tensile stiffness  $k_{n,tensile}$ , and tangential stiffness  $k_t$ . We note that overlap between envelope spheres may occur due to envelope contraction, but such interactions are not penalized. The introduction of all viscous damping parameters ( $\gamma_n$  and  $\gamma_t$ ) along the normal and tangential springs serves as regularization, used for numerical convenience. From a physical standpoint, the damping parameters may be interpreted to account for the unavoidable experimental dissipation that occurs both within the material itself (deformation of the envelope) and during the interactions between different objects (between the envelope and the particles and between particles themselves).

**Determining model parameters.** In all we have a total of 5 (between particles) + 2 (between particles and envelope spheres) + 5 (between envelope spheres) = 12 model parameters whose values are in need of determination. For the ease of parameter calibration, we further enforce several constraints in advance to reduce the dimension of calibration. These constraints are based on a combination considering common DEM practice, physical arguments and computational expenses. First, since the effect of gravity is negligible and accordingly all spheres are scaled to share the same mass with the hollow octahedrons, we set  $k_{n,p-s} = k_{n,p-p}$  and  $\gamma_{n,p-s} = \gamma_{n,p-p}$ . The choice of setting  $k_{n,p-s} = k_{n,p-p}$  also prevents excessive penetrations between the envelope and the fabric particles, avoiding unphysical long-range contacts between chain mail particles and distant envelope spheres. Second, we set  $k_{t,p-p} = \alpha \times k_{n,p-p}$ , with  $\alpha$  being a value between 0 and 1. It has been shown that for modelling flow of rigid spheres, the steady state dynamical response (for example, velocity profile and packing fraction) is not sensitive to the specific value of  $\alpha$  and to the coefficient of restitution for various tested strain rates, provided a rigid limit is ensured (that is,  $k_n$  is large enough). A smaller value of the coefficient of restitution mainly reduces the time needed to reach steady state, by dissipating kinetic energy more quickly, thereby reducing the number of time steps needed. Since we are only interested in the equilibrated states (that is, equilibrated state of isotropic compression and that of the three-point bending loading), following common DEM practice we set  $\alpha = 2/7$ ,  $e_{n,p-p} = e_{n,p-s} = 0.1$ ,  $e_{t,p-p} = 1$  ( $\gamma_{t,p-p} = 0$ ),  $e_n = 0.1$  and  $e_t = 1$  ( $\gamma_t = 0$ ). Lastly since the envelope is very compliant for both compression and shear, we assume  $k_{n,compressive} = k_t$ .

With these pre-enforced constraints, the number of parameters in need of calibration reduces to four:  $k_{n,p-p}$ ,  $\mu_{p-p}$ ,  $k_{n,compressive}$  and  $k_{n,tensile}$ . One additional parameter is the time step  $\Delta t$ . We pick  $\Delta t$  to be a small fraction of the characteristic binary collision time  $t_c = \pi \left( \frac{2k_{n,p-p}}{m_p} - \frac{\gamma_{n,p-p}^2}{4} \right)^{-1/2}$  (ref. <sup>35</sup>). As larger contact stiffness leads to smaller time steps, and thus leads to an increase of time steps required to achieve equilibrium, we do not use the true mechanical property of the material to determine the value for  $k_{n,p-p}$ , but rather we pick a value that is large enough to ensure rigid limit, such that the physical results at equilibrated states are no longer affected by the particular value of  $k_{n,p-p}$ . For spheres and

convex-shaped solid particles in general where only one contact is possible between two particles, studies have shown that picking  $k_{n,p-p} \geq 10^4 P$  is enough to ensure rigid limit, where  $P$  is the confining pressure. In our case however particles are no longer convex and are discretized into nodes and multiple contacts can occur between two particles. We choose a value for  $k_{n,p-p}$  such that the contact penetration does not exceed 1% of the truss members' thickness (0.01 mm). Since we model the envelope as a collection of interacting spheres, values for  $k_{n,compressive}$  and  $k_{n,tensile}$  must be determined together with the value of  $k_{n,p-p}$ , so that the model as a whole can capture the experimental results. In this work, we use the experimentally obtained apparent bending modulus value at the highest confining pressure ( $P = 93$  kPa) to calibrate our model. Specifically, the values of  $k_{n,p-p}$ ,  $k_{n,compressive}$  and  $k_{n,tensile}$  are determined by matching the simulated apparent bending modulus and experimental results at  $P = 93$  kPa. With these parameters being determined, we further employ a global damping ratio  $\beta = 0.001$  to facilitate the relaxation process. (The corresponding implemented global damping is  $\xi = \beta \sqrt{k_{n,p-p}/m_p}$  (ref. <sup>32</sup>)). Lastly, we set  $\mu_{p-p} = 0.25$ , a value determined by calibrating and validating against triaxial compression experiments on 3D-printed spheres<sup>36</sup>.

The calibrated values for all model parameters (Extended Data Table 3), once determined, remain unchanged throughout this study. Our simulation results show that our calibrated model is robust against different confining pressures and different initial configuration of the particles (Fig. 2a) and give a physical representation of the shape of the deformed envelope (Extended Data Fig. 2). However, we acknowledge that the values of the parameters are not unique in terms of capturing the experimental results, and they depend on the specific calibration process.

**Computing the probability distribution of normal and tangential contact forces.** The probability distribution functions are computed in their discretized form by partitioning the contact force magnitudes into bins with a uniform width, calculating the probability associated with each bin as the count of contact force in each bin divided by the total count of contact forces, and defining the force magnitude corresponding to each probability by the midpoint of each bin.

**Validating the model with other particle geometry.** To ensure that the LS-DEM model generalizes beyond the octahedral unit cell, we fabricated another sample consisting of interlocked particles constructed from three orthogonal rings. The apparent bending moduli for different confining pressures are compared between experiment and simulation (Extended Data Fig. 5a) and show good agreement.

**The power law fitting between  $E^*$  and  $\bar{Z}$ .** To fit the relation between apparent bending modulus  $E^*$  and average contact number per particle  $\bar{Z}$ , we adopted a power-law function predicted by the critical phenomenon of jamming transition<sup>13</sup>. The functional form is:

$$E^* = a(\bar{Z} - Z_0)^b.$$

Here  $a$  is the fitting coefficient,  $b$  is the scaling exponent, and  $Z_0$  corresponds to the isostatic coordination number. Since  $Z_0$  depends on the specific particle geometry, we use different  $Z_0$  values for different particle shapes, while keeping  $a$  and  $b$  the same for the fitting. The fitting parameters used are shown in Extended Data Table 1. We note that owing to the expense of the LS-DEM simulation process, we do not obtain data with enough orders of magnitude to validate the power-law scaling or to claim a power exponent. The study of a generalized scaling behaviour for particles with complex shapes and interlocking topology remains an open area of research.

**Uniaxial tensile tests of fabrics under confinement.** Since our fabrics are highly anisotropic, we numerically tested their apparent tensile moduli along various directions at different confining pressures (Figs. 2c, d

and Extended Data Fig. 5b, c). In contrast to the apparent bending moduli, the tensile moduli extrapolate to non-zero values at zero pressure owing to the resistance offered by the chain links. For the octahedral particles and particles with three orthogonal rings, the tensile moduli along the length and width directions are approximately the same, as these are also symmetry axes. However, for the cubic particles, since the symmetry axes do not fall along the samples' length or width, the tensile moduli along these two directions are different. The Poisson's ratio measured in these tensile tests are also shown in Extended Data Table 4.

**Poisson's ratio under bending and beam versus plate assumption.** To evaluate the fabrics' Poisson's ratio under bending deformation, we analysed the fabrics' curvature along length ( $\kappa_L$ ) and width ( $\kappa_W$ ) directions in LS-DEM simulation. For the octahedra fabrics at 13 kPa confining pressure, we obtained  $\kappa_L = 3.2 \times 10^{-1} \text{ m}^{-1}$  and  $\kappa_W = -2.5 \times 10^{-2} \text{ m}^{-1}$ . The Poisson's ratio under bending is then calculated as<sup>37</sup>:  $\nu_{WL} = -\kappa_W/\kappa_L = 0.078$ .

Owing to this relatively small Poisson's ratio, the difference of apparent bending modulus ( $E^*$ ) calculated using the elastic beam model (Timoshenko beam theory) versus plate model (Kirchhoff-Love plate theory) will be:  $\nu_{WL}^2 = 6 \times 10^{-3} < 1\%$ . Thus, we adopted the elastic beam model when calculating apparent bending modulus (1) for simplicity.

## Data availability

The data that support the findings of this study are available from the corresponding author upon reasonable request and online (<https://github.com/Daraio-lab/StructuredFabricsTunable-WangY>).

35. Silbert, L. E. et al. Granular flow down an inclined plane: Bagnold scaling and rheology. *Phys. Rev. E* **64**, 051302 (2001).
36. Miskin, M. Z. & Jaeger, H. M. Adapting granular materials through artificial evolution. *Nat. Mater.* **12**, 326–331 (2013).
37. Pratapa, P. P., Liu, K. & Paulino, H. Geometric mechanics of origami patterns exhibiting Poisson's ratio switch by breaking mountain and valley assignment. *Phys. Rev. Lett.* **122**, 155501 (2019).

**Acknowledgements** We thank K. Liu for discussions; A. Pate, H. Ramirez and M. Zuleta for printing the aluminum chain mails; D. Ruffatto for helping with printing early-stage prototypes; and S. Fan for assistance with photographing the 3D-printed sample in Figs. 1d, f and 4a, b. Y.W. and C.D. acknowledge support from the Foster and Coco Stanback Space Innovation fund, Facebook and the Army Research Office grant W911NF-17-1-0147. L.L. and J.E.A. acknowledge support from the Army Research Office (MURI grant number W911NF-19-1-0245). This research was carried out at the California Institute of Technology and the Jet Propulsion Laboratory under a contract with the National Aeronautics and Space Administration, and funded through the President's and Director's Fund Program. Computational resources were provided by the High Performance Computing Center at Caltech.

**Author contributions** Y.W. and C.D. designed the sample structure and the experiments. Y.W. fabricated the sample, performed the experiments and analysed experimental data. L.L. and J.E.A. designed the LS-DEM model. L.L. performed the LS-DEM simulations and analysed numerical results. D.H. printed the metallic chain mail. Y.W., L.L. and C.D. wrote the manuscript. All authors interpreted the results and reviewed the manuscript.

**Competing interests** The authors declare no competing interests.

## Additional information

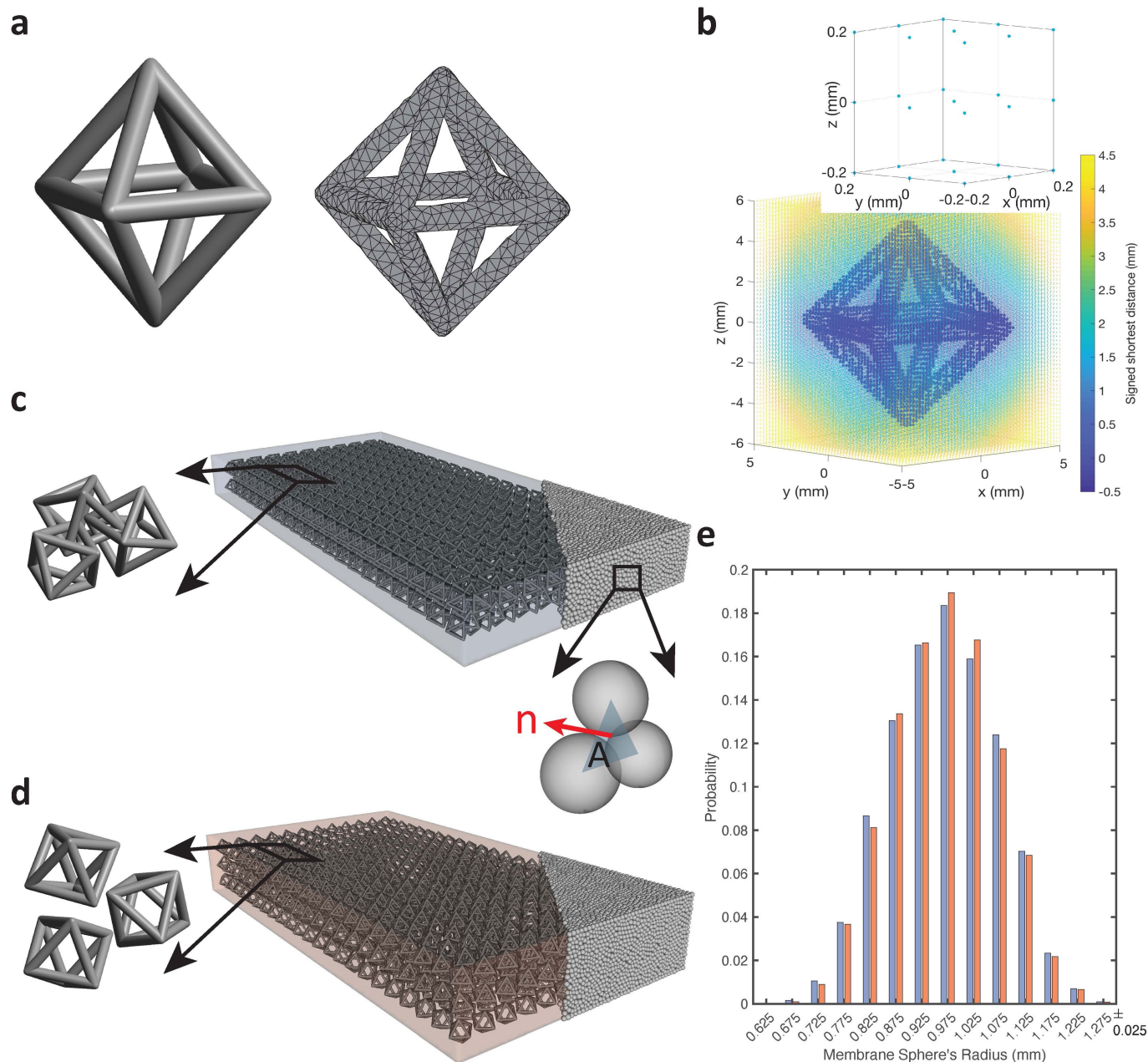
**Supplementary information** The online version contains supplementary material available at <https://doi.org/10.1038/s41586-021-03698-7>.

**Correspondence and requests for materials** should be addressed to C.D.

**Peer review information** *Nature* thanks Laurent Orgeas and the other, anonymous, reviewer(s) for their contribution to the peer review of this work.

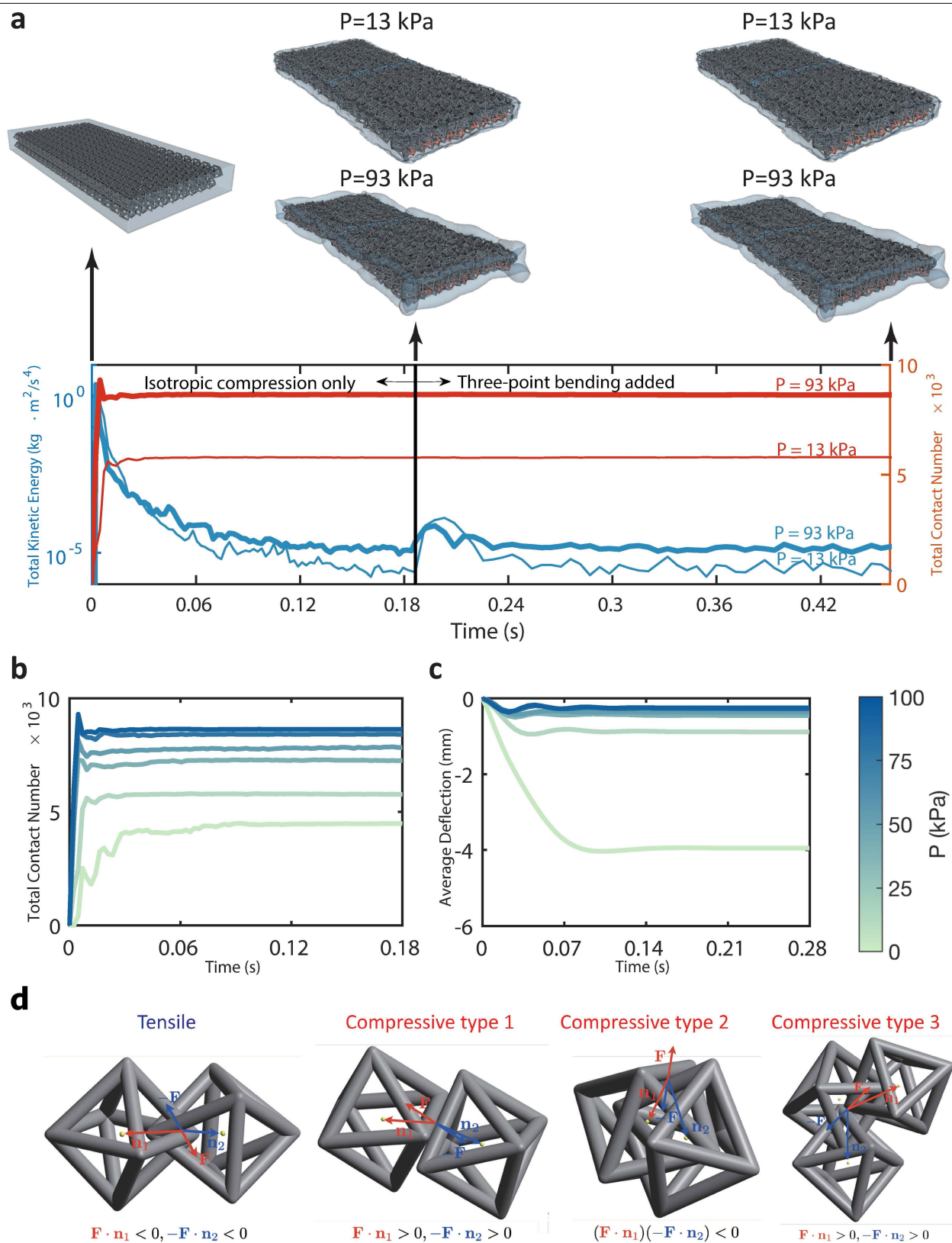
**Reprints and permissions information** is available at <http://www.nature.com/reprints>.





**Extended Data Fig. 1 | Construction of the 'digital twin' and the envelope.** **a**, The actual particle geometry (left) and the corresponding nodes and surface triangulations of the constructed digital twin (right). **b**, The corresponding 'grids' of the constructed digital twin with colour indicating the signed shortest distance to the particle surface. **c**, **d**, The initial configurations of the envelopes (represented by connected spheres) and of the granular assemblies

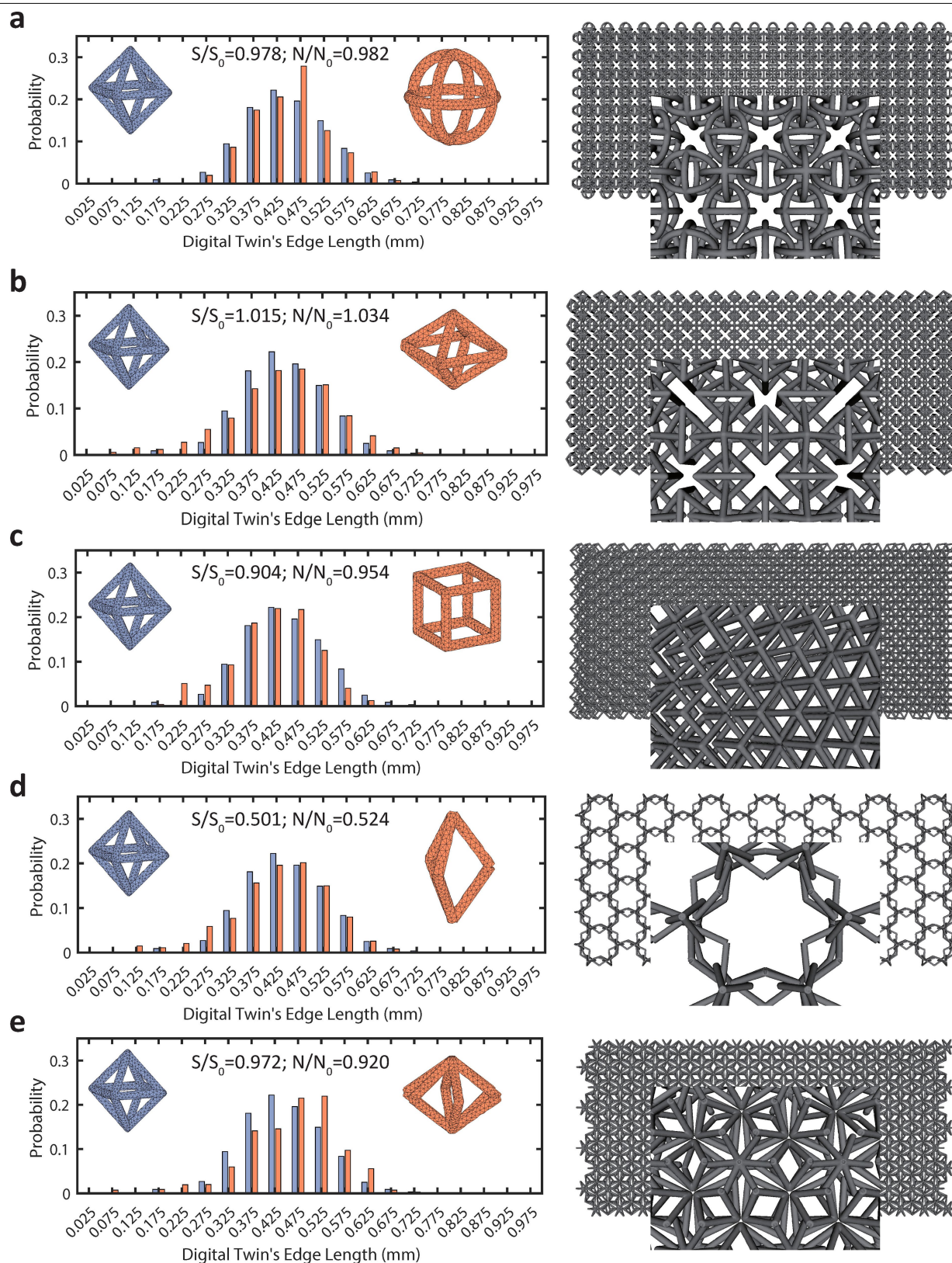
with **(c)** and without **(d)** topological interlocking. The centroids of three adjacent spheres form a triangle with surface area  $A$  and in-ward surface normal  $n$ . **e**, The probability distribution of the radii of the constituent membrane spheres of the envelope used for the interlocked fabric sheet (blue, **c**) and non-interlocked assembly (red, **d**). The notation  $\pm 0.025$  indicates the lower and upper bound for each value shown on the x axis.



**Extended Data Fig. 2 | The bending test simulation and illustration of how we categorized each contact into either the 'compressive' or 'tensile' type.** **a**, Evolution of total kinetic energy (blue) and total contact number (red) of all constituent particles of a fabric sheet under two confining pressures: 13 kPa (upper panel) and 93 kPa (lower panel). **b**, Evolution of total contact number for the same fabric sheet during the 'isotropic compression only' simulation stage

for six different applied confining pressures. **c**, Evolution of average deflection of loaded particles during the 'three-point bending added' simulation stage for the same six different applied confining pressures. **d**, In each of the subfigures,  $\mathbf{F}$  is the total contact force vector and  $\mathbf{n}_1$  and  $\mathbf{n}_2$  are vectors pointing from the contact position to the respective centroid location of each contact particle.

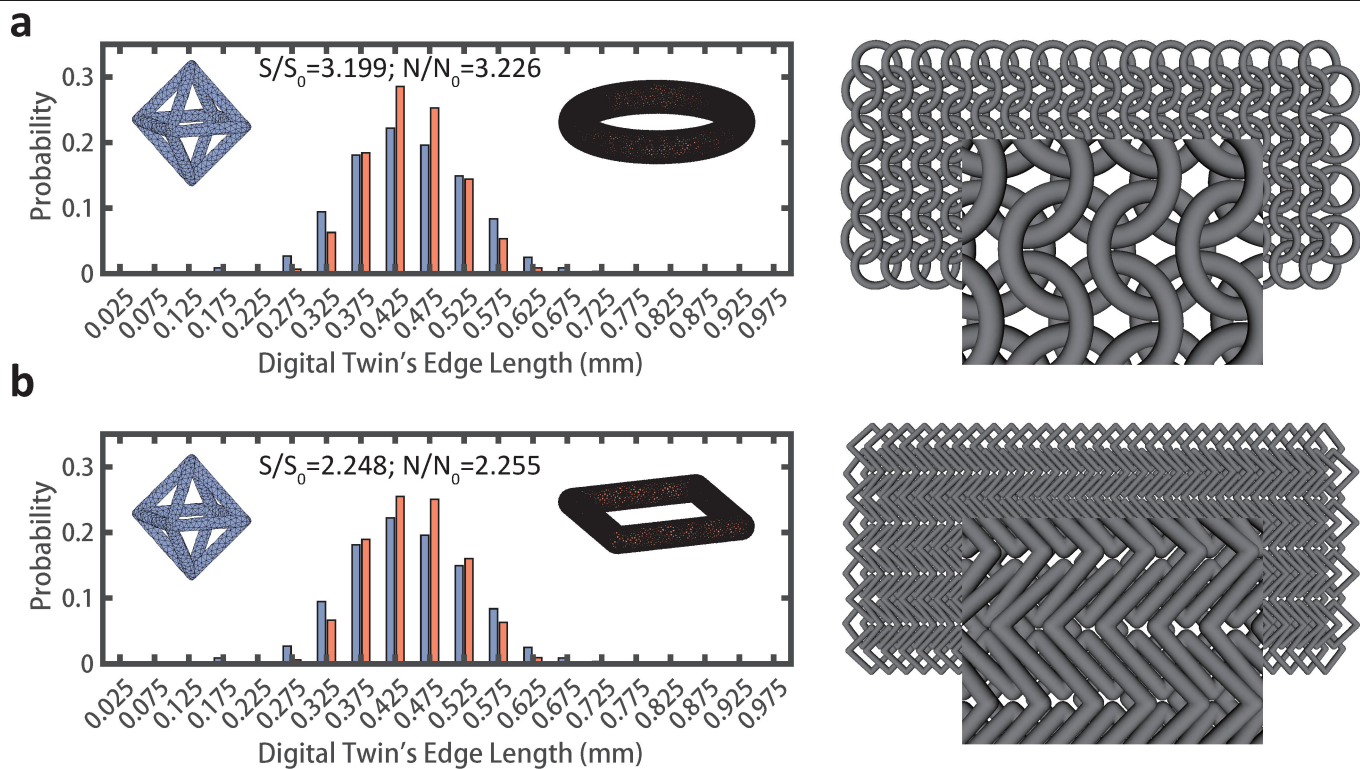




**Extended Data Fig. 3 | Details of the 3D architected particles and fabrics.** Left column, Probability distribution of the digital twin's edge lengths for all five additionally considered shapes (coloured in red) in comparison to that of the hollow octahedron (coloured in blue). In the inset,  $S$  and  $N$  represent the total surface area of the considered particle geometry and the number of nodes

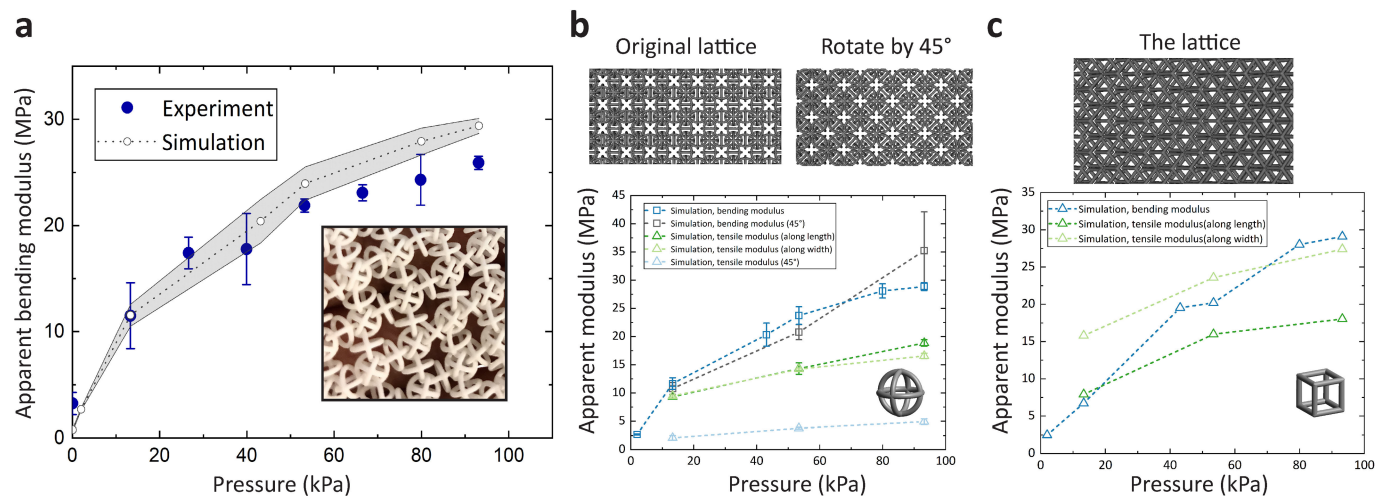
of the corresponding digital twin, respectively, while  $S_0$  and  $N_0$  represent those of the hollow octahedron and its digital twin. Right column, the corresponding assembled sheets (one layer) together with a closer look at the associated interlocking pattern.





**Extended Data Fig. 4 | Details of the classical chain mail fabrics.** The same comparison as in Extended Data Fig. 4 for classical chain mails consisting ring-shaped (**a**) and square-shaped particles (**b**). Left column, probability distribution of the digital twin's edge lengths for two different chainmail








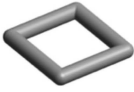
shapes (coloured in red) in comparison to that of the hollow octahedron (coloured in blue). Right column, the corresponding assembled chain mail sheets (one layer) together with a closer look at the associated interlocking pattern.



**Extended Data Fig. 5 | Comparing experimental and numerical results of two-layer fabrics consisting of particles of different shapes and loaded along different directions. a**, Comparison between experimental and simulation results on fabrics consisting of interlocking particles constructed from three orthogonal rings. **b, c**, Bending and tensile moduli along different

directions for fabrics consisting of particles constructed from three orthogonal rings (**b**) and cubic frame (**c**). The error bars shown in (a) and (b) represent the standard deviations obtained from five separate experiments and four separate simulations.

**Extended Data Table 1 | Packing fraction of different fabric sheets under various confining pressures, and fitting parameters used for the power-law relation shown in Fig. 3g**

Confining Pressure $P$ (kPa)								
93	0.164	0.159	0.192	-	0.166	-	-	-
79	0.165	0.160	0.189	-	0.167	-	-	-
53	0.165	0.160	0.188	0.103	0.169	0.143	-	-
40	0.166	0.160	0.188	0.116	0.170	0.142	0.419	0.405
25	-	-	-	-	-	-	0.418	0.404
13	0.161	0.157	0.181	0.109	0.169	0.143	0.417	0.403
2	0.155	0.152	0.175	0.09	0.161	-	0.417	0.397
Fitting Parameter $Z_0$	$4.89 \pm 0.05$ ; $5.29 \pm 0.13$ (45°)	$5.07 \pm 0.20$ ; $3.66 \pm 0.16$ (45°)	$4.68 \pm 0.20$	$4.52 \pm 0.28$	$4.24 \pm 0.12$	$5.06 \pm 0.25$	$4.03 \pm 0.16$	$4.72 \pm 0.42$
Fitting Parameters $a, b$	$a=0.159, b=2.348$							

The packing fraction in each simulation is computed as the total volume of constituent particles divided by the total occupied volume, where the total occupied volume can be computed from the overall dimensions ( $L$ ,  $h$  and  $b$ ) of the respective fabric sheet in the jammed state.



**Extended Data Table 2 | Average dimensions computed from four separate simulations**




Confining Pressure $P$ (kPa)	Length $L$ (mm)		Width $b$ (mm)		Height $h$ (mm)	
	Interlocked	Non-interlocked	Interlocked	Non-interlocked	Interlocked	Non-interlocked
93	209.87	204.39	92.34	98.41	16.11	16.95
	$\pm 0.52$	$\pm 0.86$	$\pm 0.33$	$\pm 2.14$	$\pm 0.45$	$\pm 0.66$
79	210.03	203.68	92.06	97.40	16.18	16.94
	$\pm 0.59$	$\pm 0.55$	$\pm 0.25$	$\pm 1.78$	$\pm 0.40$	$\pm 0.71$
53	210.25	201.52	91.66	96.39	16.23	16.91
	$\pm 0.40$	$\pm 0.36$	$\pm 0.41$	$\pm 2.46$	$\pm 0.40$	$\pm 0.74$
40	209.77	202.15	91.48	95.86	16.22	16.71
	$\pm 0.67$	$\pm 1.33$	$\pm 0.30$	$\pm 2.06$	$\pm 0.43$	$\pm 0.72$
13	211.03	201.97	92.38	94.54	16.42	16.88
	$\pm 0.73$	$\pm 0.42$	$\pm 0.39$	$\pm 1.27$	$\pm 0.34$	$\pm 1.02$
2	208.38	-	95.76	-	16.66	-
	$\pm 0.33$	-	$\pm 0.14$	-	$\pm 0.32$	-

The standard deviations are calculated from the varying initial configuration of both the interlocked fabrics and the non-interlocked assemblies in the jammed state.

**Extended Data Table 3 | Values of the model parameters used in this study**

Model parameters	Values
$k_{n,p-p} (k_{t,p-p} = 2/7 k_{n,p-p}) [kg/s^2]$	$9.7 \times 10^4$
$k_{n,p-s} (k_{t,p-p} = 2/7 k_{n,p-s}) [kg/s^2]$	$9.7 \times 10^4$
$e_{n,p-p} (e_{n,p-s}, e_n = e_{n,p-p})$	0.1
$e_{t,p-p} (e_{t,p-s}, e_t = e_{t,p-p})$	1.0
$\beta (\xi = \beta \sqrt{k_{n,p-p}/m_p})$	0.001
$\Delta t [s]$	$4.66 \times 10^{-7}$
$\mu_{p-p}$	0.25
$k_{n,compressive} (k_t = k_{n,compressive}) [kg/s^2]$	50
$k_{n,tensile} [kg/s^2]$	800

Extended Data Table 4 | The Poisson’s ratio obtained during uni-axial tensile tests under different pressures for fabrics with three particle geometries

								
	Poisson's ratio							
Confining Pressure $P$ (kPa)	Along length	Along width	45°	Along length	Along width	45°	Along length	Along width
93	0.195	0.173	0.440	0.245	0.199	0.515	0.118	0.168
53	0.219	0.230	0.697	0.300	0.236	0.527	0.133	0.197
13	0.369	0.259	0.768	0.369	0.250	0.593	0.192	0.310

## Terms and Conditions

Springer Nature journal content, brought to you courtesy of Springer Nature Customer Service Center GmbH (“Springer Nature”).

Springer Nature supports a reasonable amount of sharing of research papers by authors, subscribers and authorised users (“Users”), for small-scale personal, non-commercial use provided that all copyright, trade and service marks and other proprietary notices are maintained. By accessing, sharing, receiving or otherwise using the Springer Nature journal content you agree to these terms of use (“Terms”). For these purposes, Springer Nature considers academic use (by researchers and students) to be non-commercial.

These Terms are supplementary and will apply in addition to any applicable website terms and conditions, a relevant site licence or a personal subscription. These Terms will prevail over any conflict or ambiguity with regards to the relevant terms, a site licence or a personal subscription (to the extent of the conflict or ambiguity only). For Creative Commons-licensed articles, the terms of the Creative Commons license used will apply.

We collect and use personal data to provide access to the Springer Nature journal content. We may also use these personal data internally within ResearchGate and Springer Nature and as agreed share it, in an anonymised way, for purposes of tracking, analysis and reporting. We will not otherwise disclose your personal data outside the ResearchGate or the Springer Nature group of companies unless we have your permission as detailed in the Privacy Policy.

While Users may use the Springer Nature journal content for small scale, personal non-commercial use, it is important to note that Users may not:

1. use such content for the purpose of providing other users with access on a regular or large scale basis or as a means to circumvent access control;
2. use such content where to do so would be considered a criminal or statutory offence in any jurisdiction, or gives rise to civil liability, or is otherwise unlawful;
3. falsely or misleadingly imply or suggest endorsement, approval, sponsorship, or association unless explicitly agreed to by Springer Nature in writing;
4. use bots or other automated methods to access the content or redirect messages
5. override any security feature or exclusionary protocol; or
6. share the content in order to create substitute for Springer Nature products or services or a systematic database of Springer Nature journal content.

In line with the restriction against commercial use, Springer Nature does not permit the creation of a product or service that creates revenue, royalties, rent or income from our content or its inclusion as part of a paid for service or for other commercial gain. Springer Nature journal content cannot be used for inter-library loans and librarians may not upload Springer Nature journal content on a large scale into their, or any other, institutional repository.

These terms of use are reviewed regularly and may be amended at any time. Springer Nature is not obligated to publish any information or content on this website and may remove it or features or functionality at our sole discretion, at any time with or without notice. Springer Nature may revoke this licence to you at any time and remove access to any copies of the Springer Nature journal content which have been saved.

To the fullest extent permitted by law, Springer Nature makes no warranties, representations or guarantees to Users, either express or implied with respect to the Springer nature journal content and all parties disclaim and waive any implied warranties or warranties imposed by law, including merchantability or fitness for any particular purpose.

Please note that these rights do not automatically extend to content, data or other material published by Springer Nature that may be licensed from third parties.

If you would like to use or distribute our Springer Nature journal content to a wider audience or on a regular basis or in any other manner not expressly permitted by these Terms, please contact Springer Nature at

[onlineservice@springernature.com](mailto:onlineservice@springernature.com)